metals

MDPI

Article

A New Prediction Method for the Preload Drag Force of Linear Motion Rolling Bearing

Lu Liu [1,2], Hu Chen [1,2], Zhuang Li [1,2], Wan-Ping Li [1,2], Yi Liang [1,2,*], Hu-Tian Feng [1,2] and Chang-Guang Zhou [1,2,*]

[1] Department of Mechanical Engineering, Nanjing University of Science and Technology, Nanjing 210094, China
[2] The Key Laboratory of Performance Test and Reliability Technology for CNC Machine Tool, Zhangjiagang 215600, China
* Correspondence: liangyi@njust.edu.cn (Y.L.); zhoucg@njust.edu.cn (C.-G.Z.)

Abstract: Existing studies focusing on the prediction of the preload drag force of linear motion rolling bearing (LMRB) are mainly based on mathematical modeling and vibration signal analysis. Very few studies have attempted to predict the preload drag force of LMRB on the basis of the raceway morphology. A 50 km running test was performed on a LMRB to study the correlation between the preload drag force of the LMRB and the change in raceway morphology. The preload drag force variation was measured in six regions using a surface profiler on a preload drag force test bench. The variational law for raceway morphology was characterized using the surface roughness Ra, maximum peak-to-valley height Rt, fractal dimension D, and recurrence rate Rr. The correlations between these four parameters (Ra, Rt, D, and Rr) and the preload drag force were 0.645, 0.657, 0.718, and 0.722, respectively, based on the gray correlation method. Hence, Rr is recognized as the optimal characterization parameter. Through the Gaussian process regression model, a preload drag force prediction model was established. Using the recurrence rate Rr as the input parameter to develop the prediction model, the accuracies of the prediction results of the three sets are 93.75%, 98.5% and 98.8%, respectively. These results provide a new method for the monitoring and prediction of the degradation of the preload drag force of a LMRB based on rolling track topography.

Keywords: linear motion rolling bearing; preload drag force prediction; morphology characterization; fractal theory; recursive analysis

check for updates

Citation: Liu, L.; Chen, H.; Li, Z.; Li, W.-P.; Liang, Y.; Feng, H.-T.; Zhou, C.-G. A New Prediction Method for the Preload Drag Force of Linear Motion Rolling Bearing. *Metals* **2022**, *12*, 2139. https://doi.org/10.3390/met12122139

Academic Editor: Mohammad Jahazi

Received: 30 October 2022
Accepted: 30 November 2022
Published: 13 December 2022

Publisher's Note: MDPI stays neutral with regard to jurisdictional claims in published maps and institutional affiliations.

Copyright: © 2022 by the authors. Licensee MDPI, Basel, Switzerland. This article is an open access article distributed under the terms and conditions of the Creative Commons Attribution (CC BY) license (https://creativecommons.org/licenses/by/4.0/).

1. Introduction

The linear motion rolling bearing (LMRB) is widely used in machinery and precise measuring instruments of key transmission components and has high loading capacity, high transmission accuracy, and long life [1–3]. To improve the rigidity and transmission accuracy of an LMRB, clearance is usually eliminated by increasing the rolling element diameter to generate a preload [4,5]. During the operation, the increment between the rolling element and raceway gradually decreases, which decreases the preload and thus affects the transmission accuracy and CNC machine tool accuracy [6].

The preload force on an LMRB (a closed system) cannot be measured directly and is generally calculated indirectly by measuring its preload drag force (friction force). Thus, it is important to detect the degradation in preload drag force on an LMRB during service [7].

Ren et al. [8] deduced the equation relating the preload and friction coefficient of an LMRB and designed an experiment to verify that relation. Cheng et al. [9] conducted wear experiments on an LMRB and measured its frictional behavior under different external loads, preloads, speeds, and lubricant conditions and finally obtained the empirical friction equations for the LMRB. Oh et al. [10] considered the effects of material parameters, geometric parameters, assembly, and operating conditions to establish a friction model for the two-point ball contact of an LMRB. Zhou et al. [11] introduced fractal theory to describe the contact area of a rolling element and raceway from the microcontact point of view,

calculated the wear in the contact area of the rolling element and raceway, and established a preload degradation model of an LMRB. The above studies all needed to disassemble the LMRB carriage from the workbench, which is a complicated task that may degrade the accuracy of the whole system, so a large amount of research has been conducted on indirectly detecting the preload force.

To achieve online monitoring of the preload drag force on an LMRB, Huang et al. [12] decomposed and reconstructed the vibration signal, current signal, and acoustic emission signal during operation of a CNC machine tool spindle using wavelet packets. The performance degradation of the spindle system was accurately evaluated by simplifying the data using dynamic clustering and training the evaluation model through a combination of sliding window forgetting and gradient descent methods. Yang et al. [13] performed ensemble empirical mode decomposition to denoise rolling bearing vibration signals, used scattering entropy as the feature vector to construct the degradation cosine distance index, and finally assessed bearing performance degradation via the cosine distance health threshold. Chen et al. [14] used the software ADAMS to simulate an LMRB with different preloads to obtain their inherent frequencies and vibration patterns of each order. The hammer impulse method was used to verify the results, which showed that the preload is positively correlated with the inherent frequency of each order. However, the above methods are susceptible to noise and identify the preload with low resolution.

Because the raceway topography directly reflects the wear of an LMRB rolling element and raceway, there is no need to separate the carriage from the table to measure the raceway topography. The LMRB slider can move back and forth together with the table along the guide; therefore, it can be used to monitor the preload drag force by measuring the wear of the raceway surface. However, owing to the long time needed for a wear experiment and the lack of large loading equipment as support, there are few studies characterizing the degradation of preload drag force of an LMRB through the raceway wear. The relevant research has mainly investigated material wear laws. Liu et al. [15] investigated the correlation between surface topography and mechanical properties measured at the micron/nanometer scale using a tribological probe microscope (TPM) that could simultaneously measure the surface topography, friction, Young modulus, and hardness. They found that surface geometric features have a modulating effect on mechanical properties. Valtonen et al. [16] simulated the frictional wear of a loader bucket under realistic conditions in a laboratory and characterized the wear surface cross sections of the service blade and the experimental specimen using optical microscopy and scanning electron microscopy. This experiment provided an accurate simulation of actual bucket wear. Zhang et al. [17] investigated the wear and contact fatigue of modified involute gears under minimal lubrication. The degrees of wear at different locations were compared through the change in surface profile before and after the experiment. Hanrahan et al. [18] investigated the wear mechanism of micromachined ball bearings with different coating materials and analyzed the bearing raceway wear using Raman spectroscopy, scanning electron microscopy (SEM), and optical microscopy. Zuo et al. [19] introduced the single fractal and multiple fractal methods to describe the dynamic evolution of the brass surface during wear using the fractal dimension D and multiple windrow spectral width $\Delta\alpha$. Xiong et al. [20] investigated the surface morphology, residual stresses, and fatigue life of a metal matrix composite and characterized its surface morphology using two-dimensional and three-dimensional roughness. Zhu et al. [21] introduced recursive analysis to study the roughness profile of Cu-30% Zn wear surfaces and described their nonlinear dynamic evolution using recurrence plots and two recurrence parameters.

As shown in Figure 1, this paper characterizes the LMRB full-service cycle according to the change in raceway morphology, based on which a new prediction method for the preload drag force of LMRB can be built on the basis of the raceway morphology characterization. The paper is structured as follows. The Section 2 introduces the loading test bench, preload drag force test bench, raceway morphology measurement device, and test parameter setting for the LMRB. The Section 3 analyzes the preload degradation

and change in raceway morphology and quantifies the law characterizing the change in raceway morphology using statistical parameters, single fractals, and recursive analysis. The Section 4 discusses the relationship between the preload drag force and parameters used to characterize the raceway morphology in terms of mapping and describes the strength of the correlation using gray correlation analysis. The Section 5 establishes the preload drag force prediction model of LMRB based on Gaussian process regression, Finally, conclusions are drawn in the Section 6. The technical route of the research is shown in Figure 1.

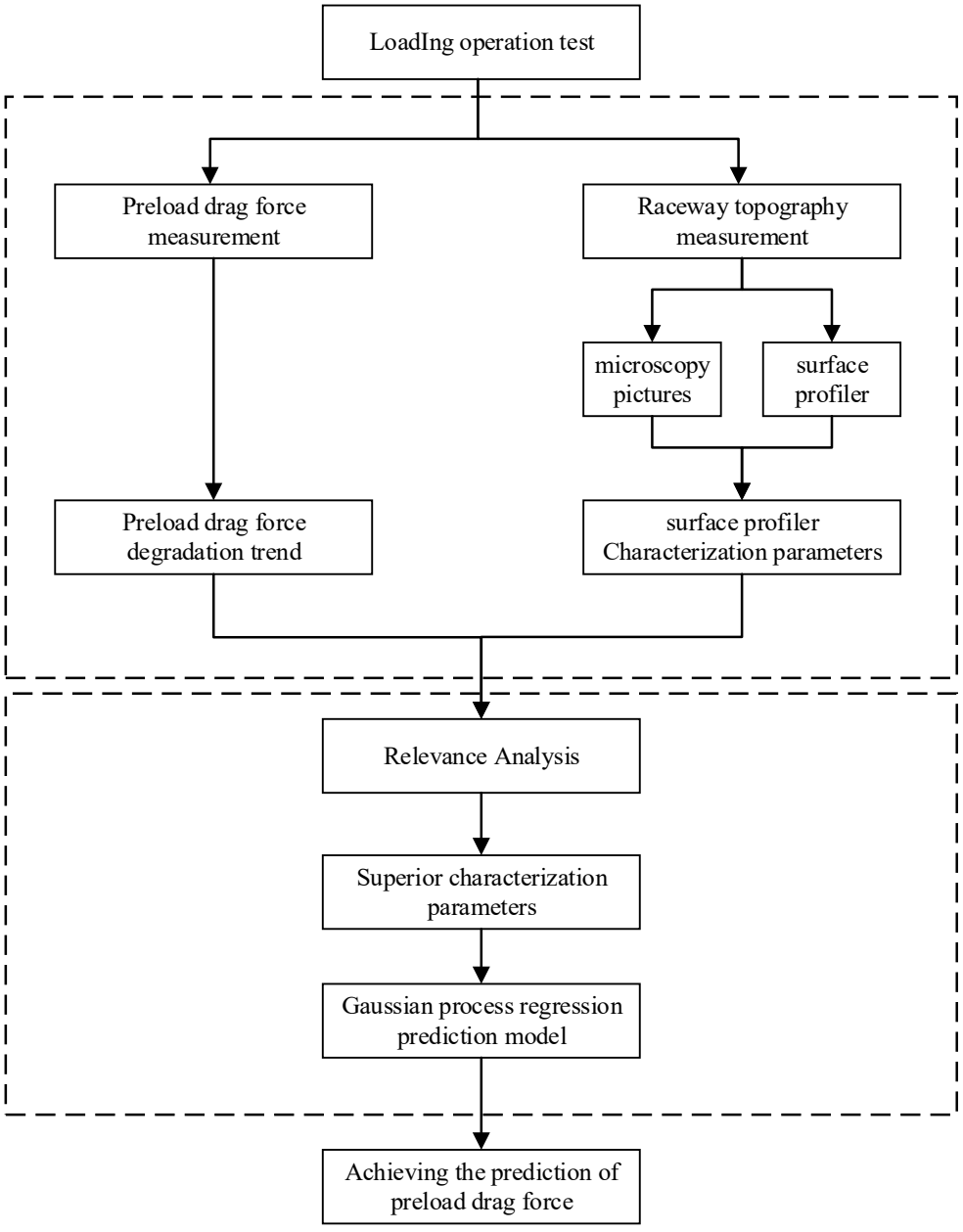


Figure 1. The structure diagram of this research.

2. Experiment

A typical LMRB (model DZ35ZC2H2, Hanjiang Machine Tool, Shaanxi, China) was used to test loading, measure preload drag force, and measure raceway topography. The LMRB parameters are shown in Table 1.

Table 1. LMRB parameters.

Parameter	Symbol	Value/Unit
Basic dynamic load rating	C	58 kN
Diameter of the rolling element	D	4 mm
Length of rolling element	l	6 mm
Basic static load rating	C_0	135 kN
Hardness of raceway	H	58 HRC
Guide material	\	GCr15
Carriage material	\	GCr15
Rolling element material	\	GCr15
Length of the tested rail	L	1480 mm

2.1. Loading Test

As shown in Figure 2, the main body of the test bench consisted of a bed frame, a gantry loading device, a rack and pinion (②, ③), two guide rail pairs (⑦), a servo motor (①), and a guide adapter plate (⑧). The gantry loading device consisted of a hand wheel (⑥), a pad (④), and force sensors (⑤). Two LMRBs were bolted to the adapter plate of the test bench via wall-mounting. The carriage was loaded vertically through the hand wheels on both sides of the gantry, and the magnitude of the applied load was tested and transmitted to a data acquisition system through an FN3000-A2 force sensor on the loading block. Powered by the servo motor, the gantry was driven by the rack and pinion to realize reciprocating motion of the carriage on the guide rail. Designing the experimental protocol for the loading operation mainly involves determining the loading stress, running speed, measurement mileage interval, and cutoff conditions. The parameters of this experiment are shown in Table 2.

Table 2. Experimental parameters.

Loading and Running Text	
Loading	34.8 kN
Running speed	50 m/min
Measurement interval	5 km (0–30 km), 10 km (>30 km)
Lubrication method	Grease lubrication(glp-500)
Experiment temperature	20 ± 0.5 °C
Running distance	1000 mm
Safety distance	480 mm
Preload drag force measurement text	
Sliding table moving speed	0.7 m/min
Measuring length	1000 mm
Sampling frequency	10 Hz
Raceway topography measurement text	
Range of surface profiler	100 μm
Gaussian filter cutoff point of surface profiler	0.25 mm
Resolution of surface profiler	0.01 μm
Measuring length	2.5 mm
Sampling points	4500

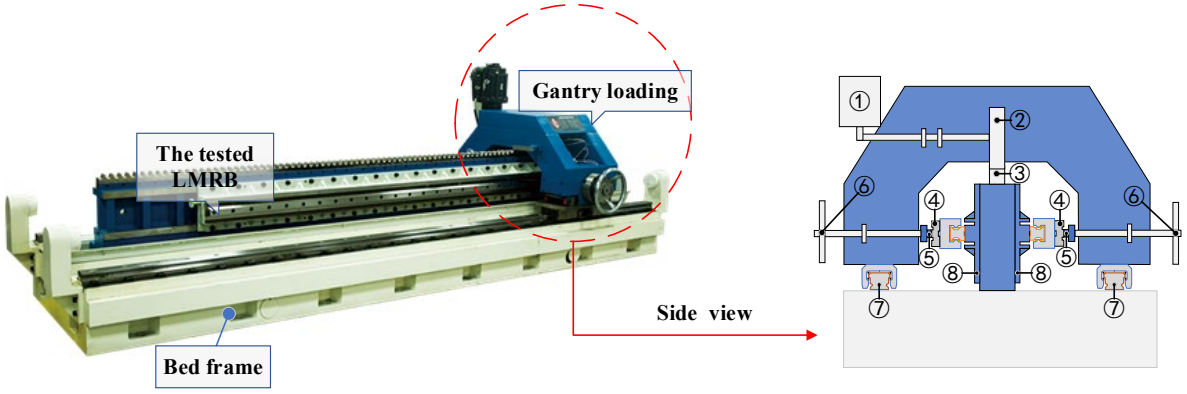


Figure 2. Loading test bench.

2.2. Preload Drag Force Measurement

As shown in Figure 3, the preload drag force test bench consisted of a bed frame, sliding table, dynamometer, PC, rack and pinion, and spacer. The sliding table moved on the guide rail with a speed of 0.7 m/min and was driven by the servo motor, which drove the dynamometer to push the carriage of the testing rail. The dynamometer recorded the drag force in real time and transmitted it to the PC. This measurement process was repeated six times (three times forward and three times backward). The first 5% and the last 5% of the measured signals were removed, and the average of the middle 90% of the data was taken as the preload drag force of the LMRB. The parameters of this experiment are also shown in Table 2.

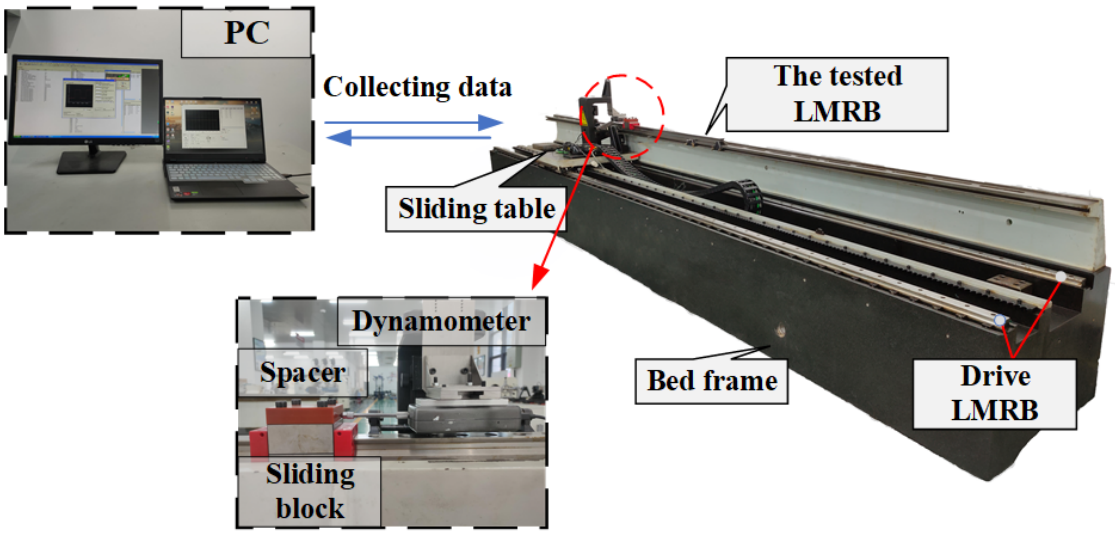


Figure 3. Preload drag force test bench.

2.3. Raceway Topography Measurement

The device for measuring surface topography consisted of a Taylor Hobson surface profiler (Surtronic S128, Taylor Hobson, UK), two V-blocks, and a data acquisition device, as shown in Figure 4. Six regions (5 mm × 10 mm) of the guide rail raceway were selected, which corresponded to the 9th, 13th, 18th, 21st, 26th, and 30th bolt holes from left to right. Three positions were selected for each region, and each position was measured three times. The scanning direction of the stylus is the Ox direction in the Figure 4. Eventually, nine two-dimensional contours were obtained to represent the surface topography of each region. During the test, the LMRB was placed on top of the V-block, and the surface profiler was placed on top of a rigid platform. The height of the stylus was adjusting to fit the tested

LMRB raceway. After that, optical microscopy pictures of the guide raceway were taken, as shown in Figure 5. The parameters of this experiment are shown in Table 2.

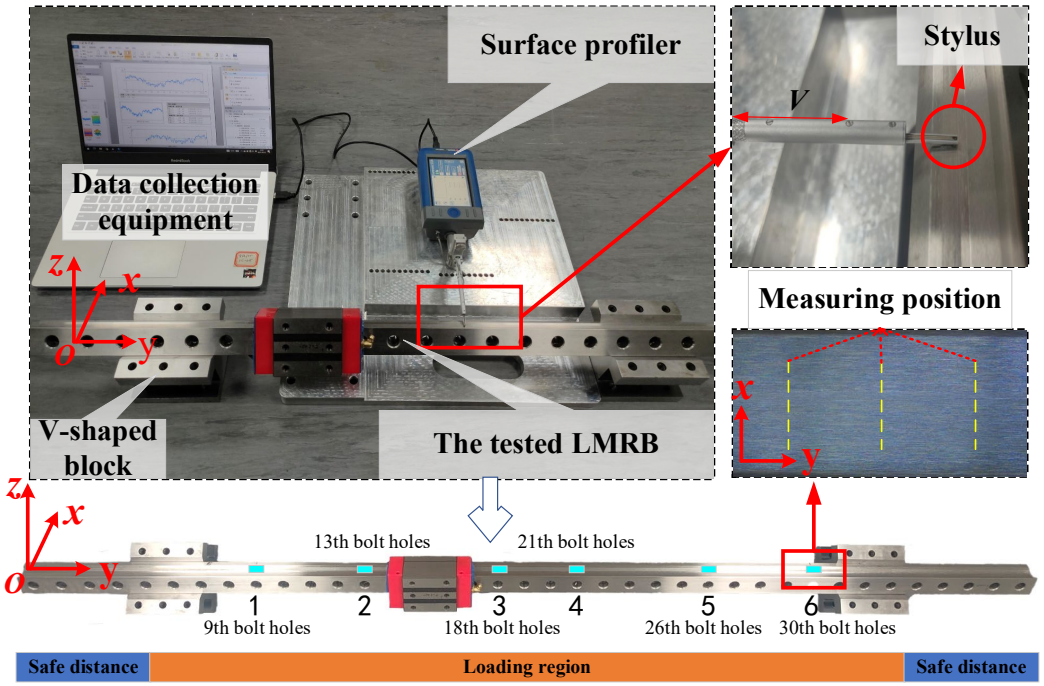


Figure 4. Device for measuring surface topography.

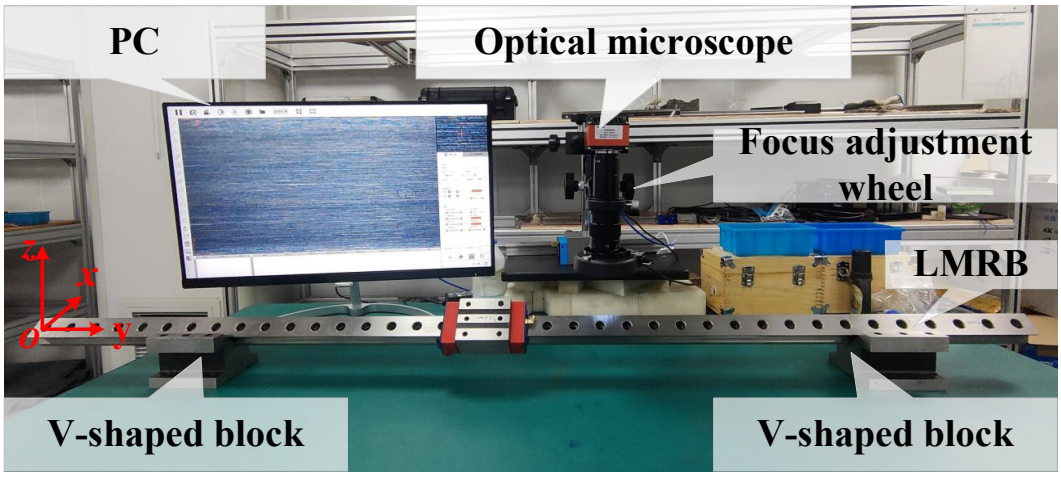


Figure 5. Micrograph measuring device.

2.4. Test Procedure

The test was mainly divided into two parts: the LMRB loading test and the parameter measurement, as shown in Figure 6.

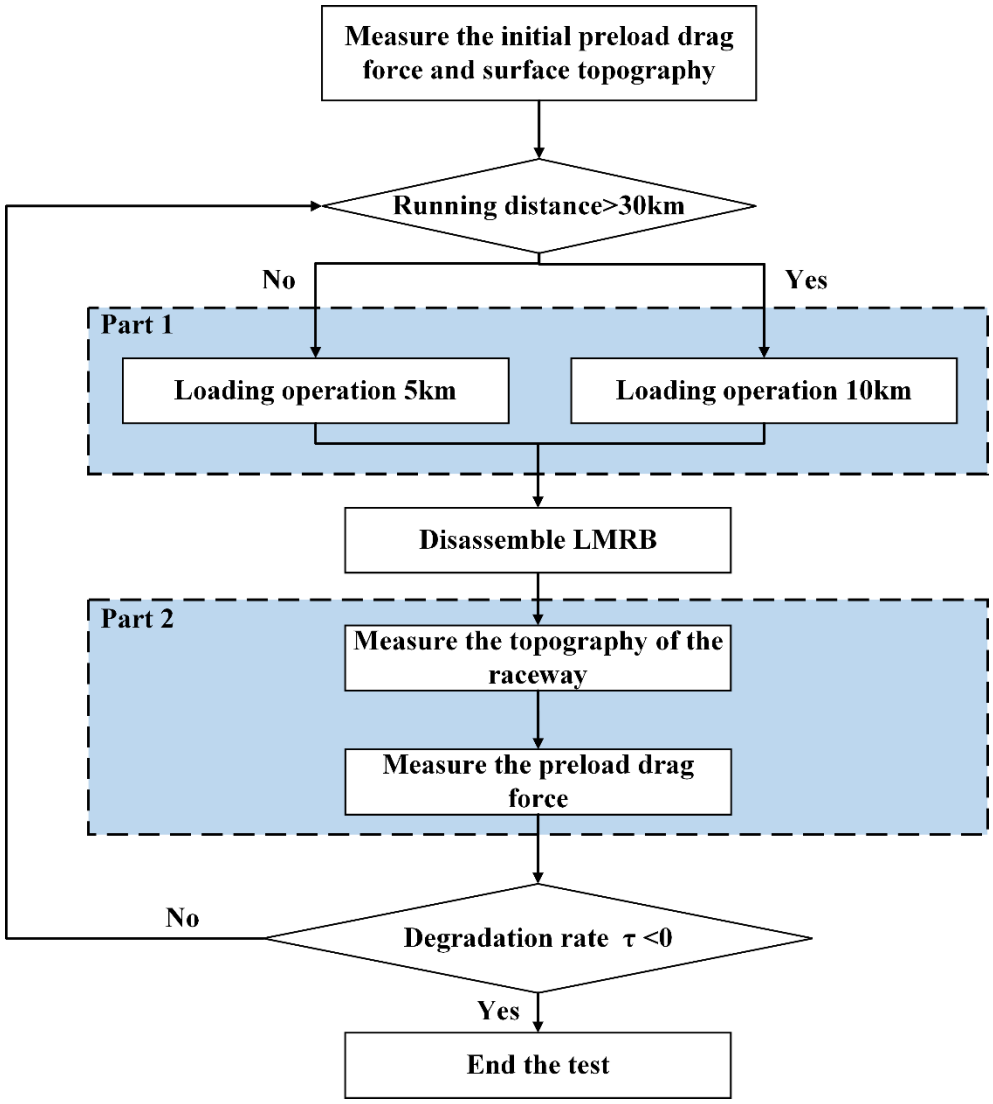


Figure 6. Test process.

3. Results

3.1. Preload Drag Force Degradation

Figure 7 shows the degradation curve of the preload drag force at 0–70 km. The preload drag force first decreases rapidly, then decreases slowly, and finally fluctuates, showing an overall exponential decrease. The reason is that there is a geometric error between the rolling element and the raceway at 0–5 km, and the contact force between the rolling body and the raceway is not evenly distributed, resulting in a large amount of wear. At 5–40 km, the geometric error is already negligible, and the wear of the rolling element and raceway is stable. At 40–50 km, the main factor affecting the preload drag force is the sliding friction between the rolling element and the guide, and the preload drag force rises significantly, which indicates that the quality of the raceway starts to deteriorate. At 50–70 km, the experimental results begin to fluctuate, but the fluctuations are all larger than at 40 km, so it is reasonable to consider this stage as the failure stage.

Under our experimental conditions, the theoretically calculated fatigue life of this LMRB should reach 285 km, while the fatigue on the raceway surface occurs only at 50 km. This difference can be explained by the effect of machining errors and geometric errors on the operation performance of LMRBs. Since the life formula is derived without taking into account all kinds of manufacturing errors, the load distribution of LMRB is considered to be

ideally uniform. During actual operation, the performance of LMRB is affected by several machining errors and geometric errors, including waviness of the rail and the carriage, groove center distance errors of the rail and carriage, the diameter error of ball and the straightness error of rail, etc. [22–24] As a result of these errors, the load applied on each roller is different, which greatly affects the actual operating life of LMRB [25] Therefore, the actual dynamic load capacity and the duration of life are much lower than those calculated in this formula. For that reason, the actual operation life in this paper differs from the calculated theoretical value. Since the focus of this study is the changes of preload drag force and surface morphology during normal operation, the results during 0–50 km are chosen and analyzed in the following sections.

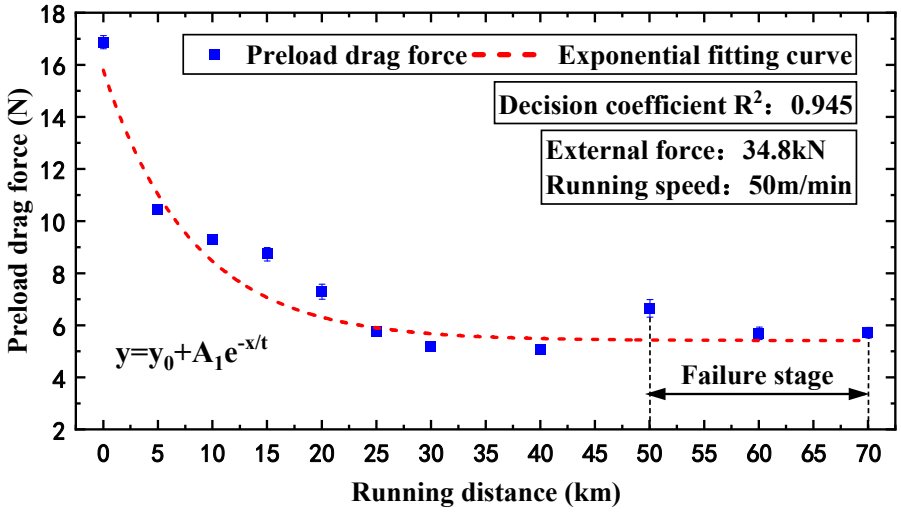


Figure 7. Preload drag force degradation curve.

Figure 8 shows the original measured signals for the preload drag force at 0 km, 40 km, and 50 km. The fluctuation of the measurement curve at 50 km rises sharply compared with that at 40 km. This indicates that the stability of the carriage motion on the guide rail dropped abruptly at 50 km, which reflects the sharp deterioration of the raceway surface quality from the side. From the results, the degradation in preload drag force of the LMRB can be divided into three stages: fast decline, slow decline, and failure. This conclusion will be further verified later.

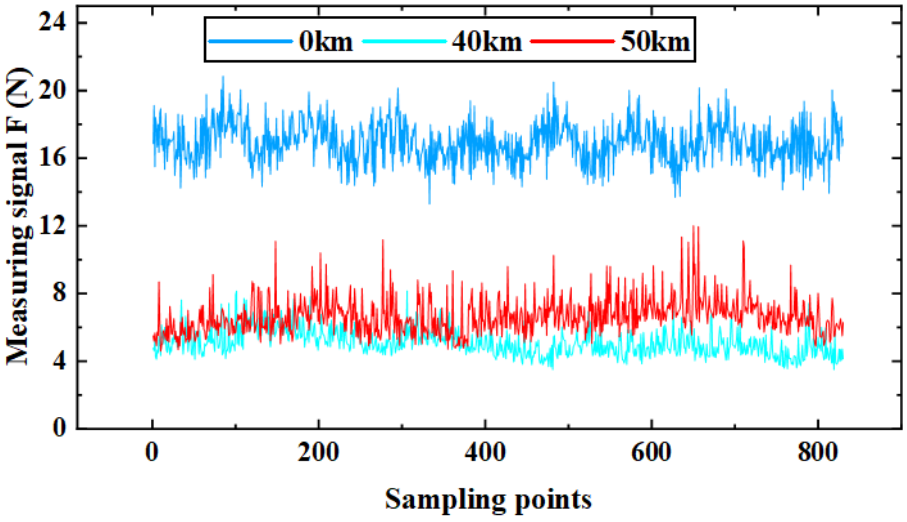


Figure 8. Original measured preload drag force.

3.2. Change in Raceway Topography

Figure 9 shows the microscopic pictures and corresponding two-dimensional surface profiles of the six raceway regions. The results are similar for the six regions; thus, only region 4 is shown below. Figure 9(a1–a9) shows the micrographs of the raceway surface from 0–50 km, and the wear area is indicated by the green line. Meanwhile, a 2D profile of the raceway surface from 0–50 km can be seen in Figure 9(b1–b9). From Figure 9(a1), it can be seen that on the original raceway, there are obvious transverse stripes, which is due to the last step of the raceway machining process being finish grinding. Correspondingly, the 2D profile of the raceway surface in Figure 9(b1) appears to be uniform before running. Compared to Figure 9(a1), the color of the wear area shown in Figure 9(a2) deepens after running for 5 km, which represents the continuous wear occurring on the contact area between the rolling element and the raceway. As Figure 9(b2) depicted, the 2D profile of the raceway surface becomes more compact and fine compared to Figure 9(b1), which can be explained thusly: With the continuous wear occurring, the larger peaks and valleys on the raceway are eliminated, and the surface quality is improved. In the subsequent 5–20 km, the LMRB was in the stable wear state and the surface micrograph and raceway profile showed little difference. At 25 km, a small amount of pitting can be clearly seen in Figure 9(a6). These pits are formed on the raceway after the wear chips have been repeatedly rolled over. In Figure 9(b6), there is no significant change in the 2D profile of surface raceway because the measurement position is fixed and does not detect the pitting intentionally. From 25–40 km, the number of pits gradually increased (Figure 9(a6–a8)), while the surface profile measured at several fixed locations did not change significantly (Figure 9(b6–b8)), indicating that the pitting had not extended to the entire raceway area during this phase. As shown in Figure 9(a9), large amounts of pitting and spalling appeared on the raceway surface along with a significant increase in the amplitude of the surface profile, indicating that the raceway surface had been severely damaged.

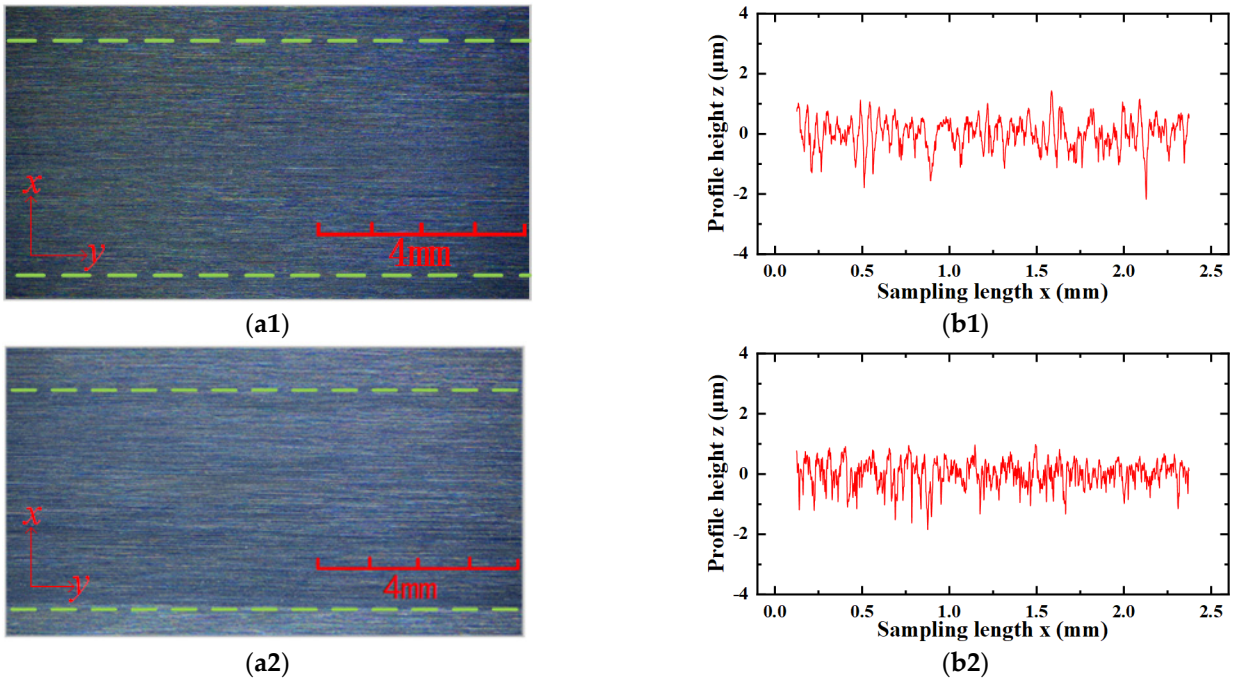
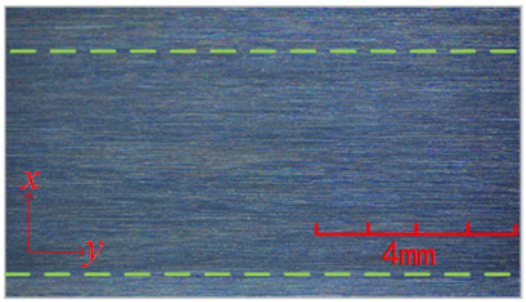
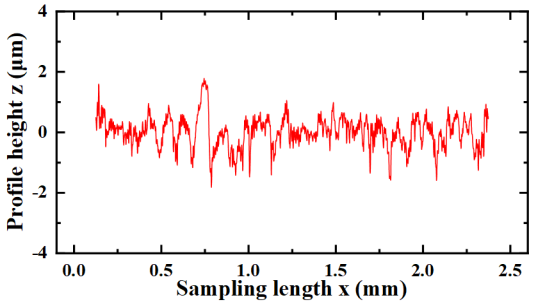


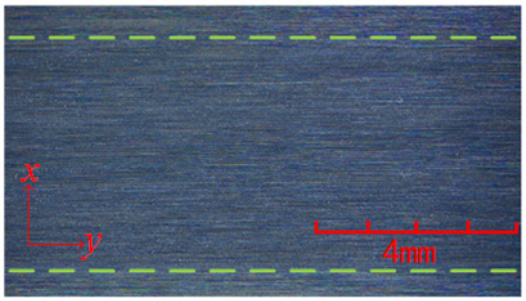
Figure 9. *Cont.*



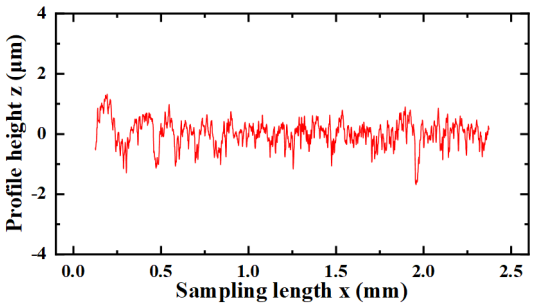
(a3)



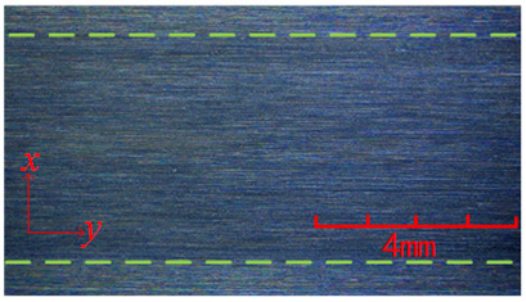
(b3)



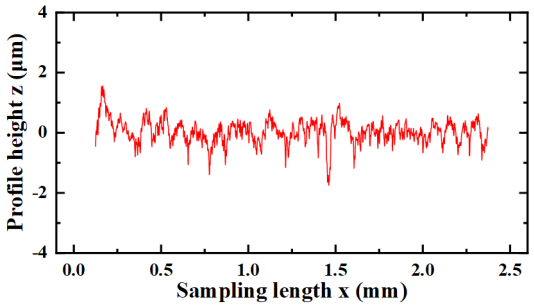
(a4)



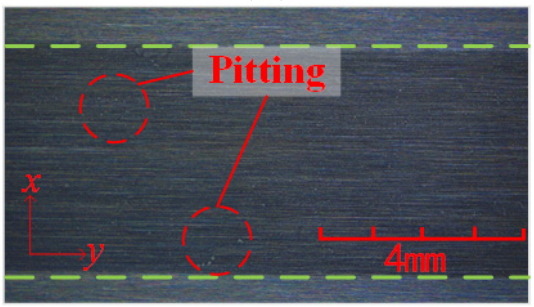
(b4)



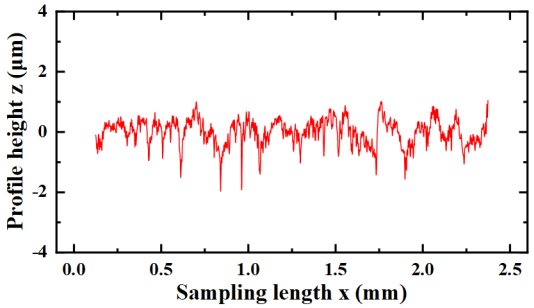
(a5)



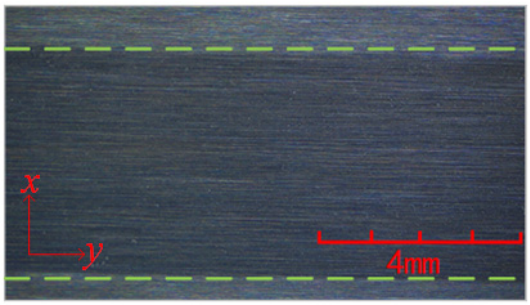
(b5)



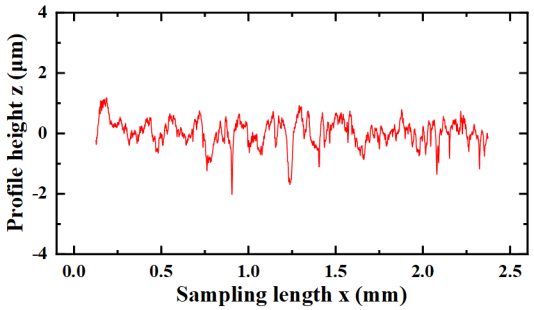
(a6)



(b6)



(a7)



(b7)

Figure 9. *Cont.*

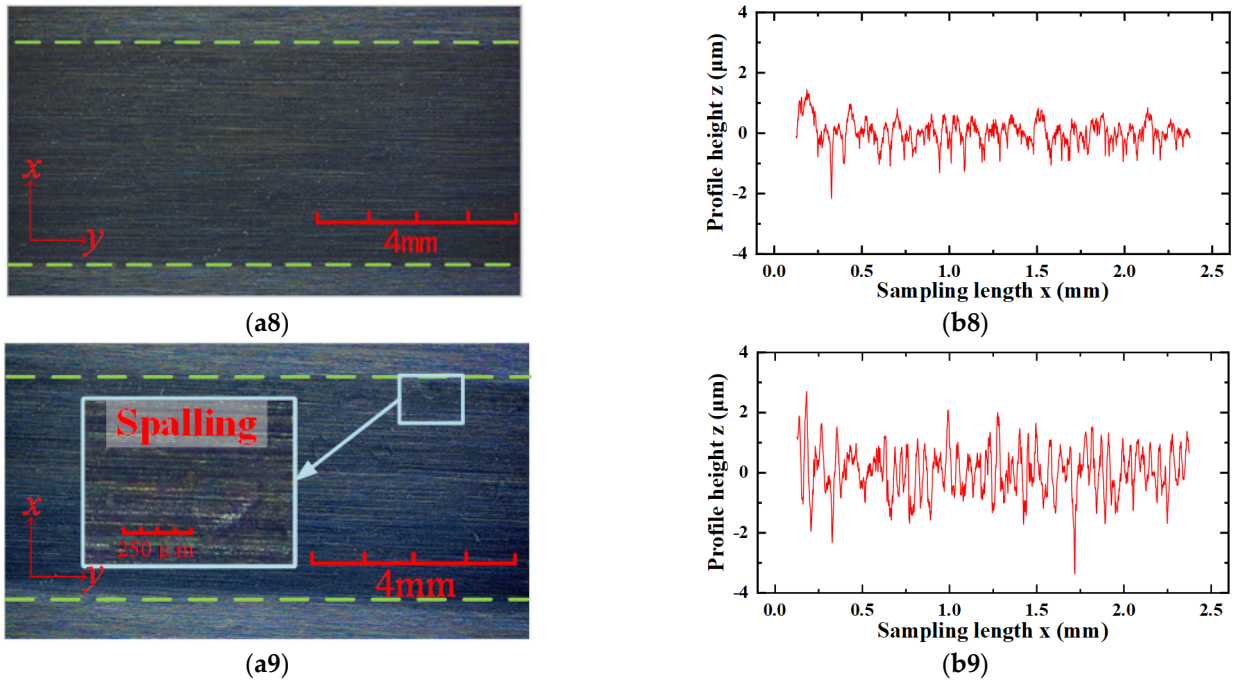


Figure 9. Microscopic pictures and two-dimensional contours of the rail raceway surface. (**a1**) and (**b1**) 0 km, (**a2**) and (**b2**) 5 km, (**a3**) and (**b3**) 10 km, (**a4**) and (**b4**) 15 km, (**a5**) and (**b5**) 20 km, (**a6**) and (**b6**) 25 km, (**a7**) and (**b7**) 30 km, (**a8**) and (**b8**) 40 km, (**a9**) and (**b9**) 50 km.

3.3. Two-Dimensional Profile of a Raceway Surface

To explore the rules more clearly, this section characterizes the two-dimensional profile of the surface and quantitatively analyzes the laws of change in raceway morphology in the six regions.

3.3.1. Statistical Parameters

The most common parameters used to describe the two-dimensional profile are the Ra and Rt [25]. Ra refers to the profile arithmetic mean deviation, and Rt refers to the maximum peak-to-valley distance of the surface profile height, which are not subjectively influenced by the profilometer. The greater the Ra and Rt, the less stable and more volatile the surface profile is. These two characterization parameters are given by

$$Ra = \frac{\int_0^L |z(x)|dx}{L} = \frac{1}{n}\sum_{i=1}^{n}|z_i| \quad (1)$$

$$Rt = |z_{max} - z_{min}| \quad (2)$$

where n is the number of sampling points, L is the sampling length, $z(x)$ is the height function of the measurement profile, z_{max} is the maximum value of surface profile height, and z_{min} is the minimum value of surface profile height.

Ra and Rt are calculated and averaged for the nine two-dimensional contours of the surface in each region to represent its variational law. By comparing the fitting effects of various fitting methods, Figure 10 presents the trends of Ra and Rt during the degradation of the preload drag force with a fifth-order polynomial fit. The fitted curve first decreases, then smooths out, and finally rises sharply, showing a "bathtub shape". When the experiment is not running, Ra for the six LMRB regions is in the range 0.35–0.4 μm, and Rt is in the range 3.0–3.5 μm. With the experiment running, Ra stabilizes at 0.25–0.4 μm and Rt stabilizes at 2.5–4.0 μm. When the experiment reaches 50 km, there is a significant increase in both Ra and Rt. At the same time, there is a slight drop in Ra both after the run and at 5 km. This

finding is consistent with that from the micrographs and two-dimensional surface profiles in the previous section.

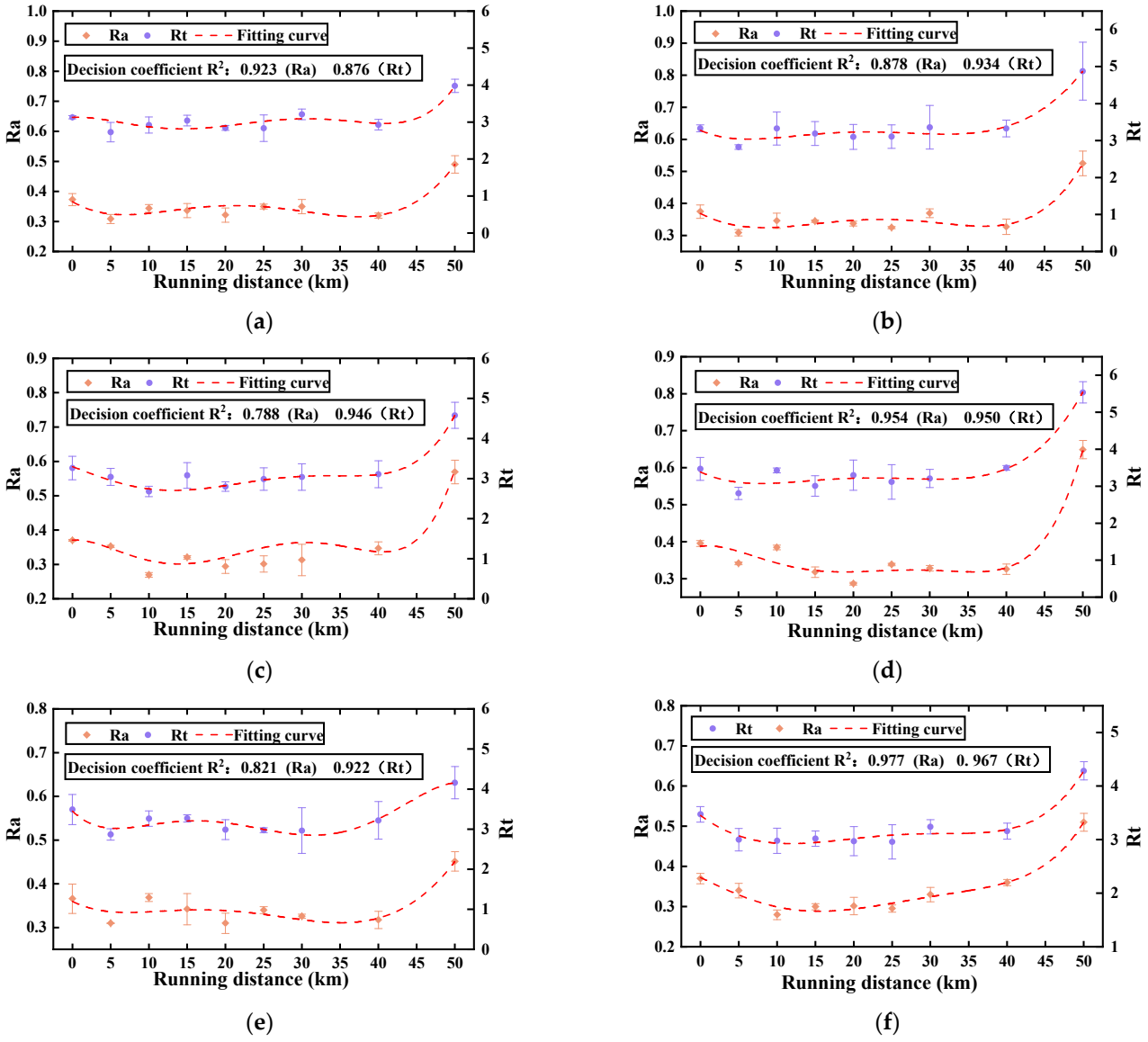


Figure 10. Evolution of the arithmetic mean deviation of the contour and maximum peak-to-valley height of the profile during wear. (**a**) Region 1, (**b**) Region 2, (**c**) Region 3, (**d**) Region 4, (**e**) Region 5 (**f**) Region 6.

3.3.2. Fractal Parameters

Since rough surfaces are multi-scale in nature and may have the same Ra, Rt for different rough surfaces depending on the instrument measurement resolution and sampling length, this section introduces a scale-independent characterization parameter that is not affected by the instrument resolution. Fractal theory has been widely used to characterize various topologies because of the self-similarity and scale invariance of frictional surfaces. This method describes the surface profile independently of the precision of the measuring instrument and has high generality [25–27]. This section uses a structure function to calculate the fractal dimension. The basic principle of the structure function is to consider a rough surface profile with fractal characteristics as a time series $z(x)$. The structure function of this time series is

$$S(t) = \langle [z(x+t) - z(x)]^2 \rangle = ct^{(4-2D)} \quad (3)$$

where $[\cdot]^2$ refers to the arithmetic mean of the differential, t denotes the interval between any two data, $\langle \cdot \rangle$ denotes the mean, and c is a constant. For each different time interval t, the corresponding $S(t)$ can be calculated using $z(x)$, and then the logS(t)–logt curve is generated. A line is fitted through the most linear part of this curve, and the slope of the fitted line is denoted as k. Then, the fractal dimension of the two-dimensional contour of the rough surface is calculated as $(4 - k)/2$.

An example of a surface two-dimensional profile $z(x)$ is presented in Figure 11. The image of the function logS(t)-logt is calculated by Equation (3), as shown in Figure 11. By fitting the linear region in Figure 11, the slope K is obtained as 0.8382, from which the fractal dimension of $z(x)$ can be calculated as 1.58.

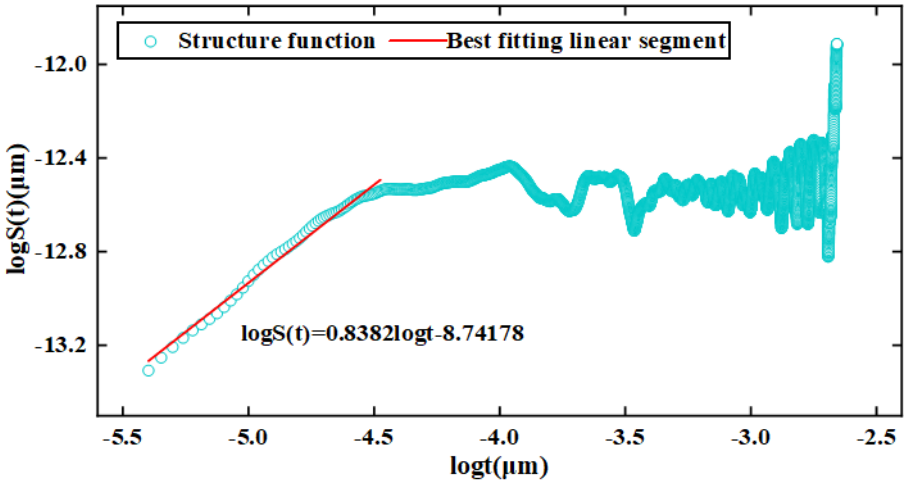
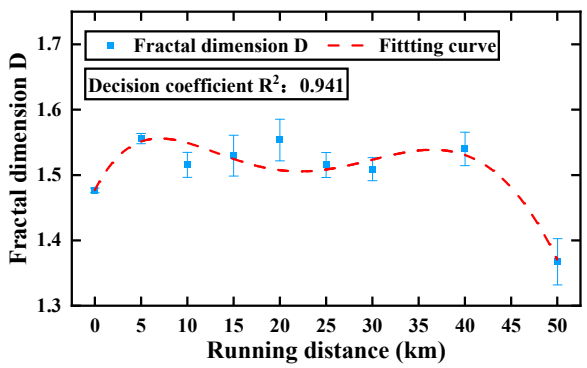
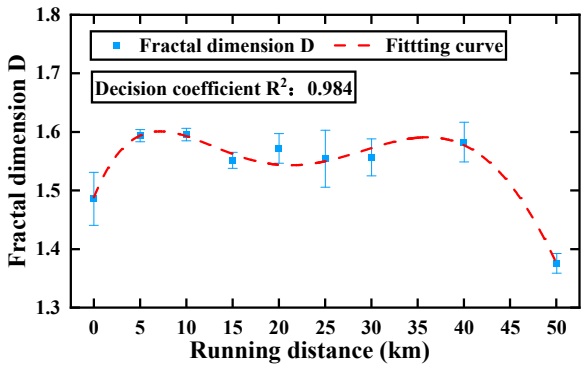


Figure 11. Structure function of the raceway surface profile in Ox direction.

Figure 12 presents the variation in fractal dimension D in the six regions. The fractal dimension of each region rises first, then smooths out, and finally drops sharply, which is the opposite trend of Ra and Rt. The fractal structure is simpler and the surface quality poorer when the fractal dimension D is smaller [28]; when D is larger, the surface structure is finer and the surface quality better. Therefore, the surface quality of the raceway improves from 0 to 5 km. At 5–40 km, the surface quality of the raceway is stable. At 40–50 km, the surface quality of the raceway deteriorates sharply. This is consistent with the conclusion from the micrographs.



(**a**)



(**b**)

Figure 12. *Cont.*

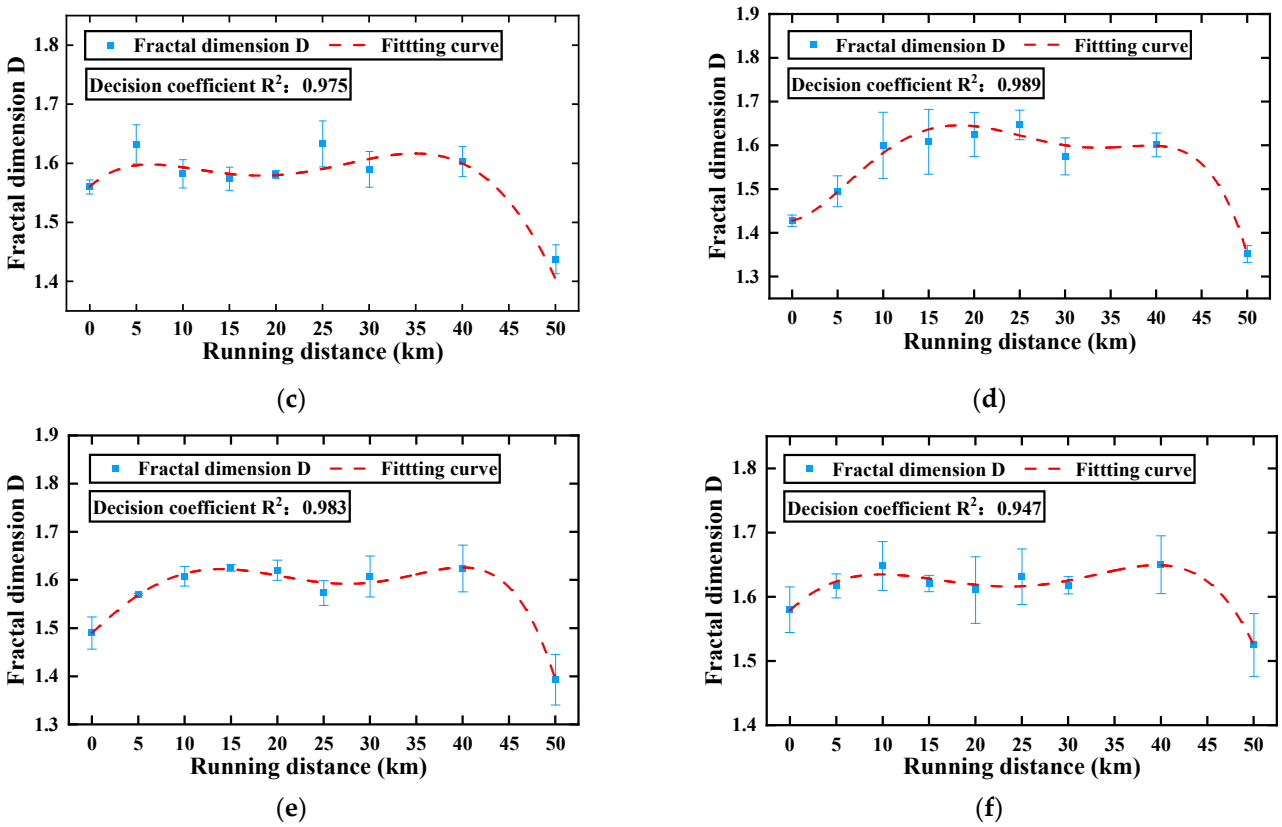


Figure 12. Evolution of the fractal dimension during wear. (**a**) Region 1, (**b**) Region 2, (**c**) Region 3, (**d**) Region 4, (**e**) Region 5, (**f**) Region 6.

3.3.3. Recursive Analysis

Recursive analysis is often used to study changes in the internal structure of a system. A recursive state is some state of the system that has similar properties to the initial state after a certain time or displacement [25]. Recurrence analysis mainly consists of two forms: recurrence diagram and recurrence rate. Recurrence diagram can visually describe the internal structural changes of the wear surface, and recurrence rate can quantitatively reflect the fluctuation stability of the wear surface. The following is an introduction to the method of drawing recurrence diagrams and the method of calculating recurrence rates.

Let the height of each point on the two-dimensional profile of the raceway surface be recorded as $z_1, z_2, z_3, z_4, \ldots, z_N$, where N is the number of sampling points. The height gap between any two points on the surface profile can be expressed as

$$r_{ij} = \left| z_i - z_j \right|, \tag{4}$$

where $i, j = 1, 2 \ldots, N$ and $|\cdot|$ is a parameter that goes to infinity.

The recurrence matrix is an $N \times N$ square matrix, and the values of the ith row and jth column of the matrix can be expressed as

$$R_{i,j}(\varepsilon) = \theta\left(\varepsilon - r_{ij}\right), \tag{5}$$

where ε is the threshold value, usually taken as 0.5σ, where σ is the standard deviation of the data set; $\theta(\cdot)$ is the Heaviside step function given by

$$\theta x = \begin{cases} 0, & x \leq 0 \\ 1, & x > 0 \end{cases}. \tag{6}$$

Because $R_{i,j}$ has the values 0 and 1, the recursive matrix is a binary symmetric matrix. When $R_{i,j} = 1$, the height gap between the two points on the two-dimensional profile of the guide track surface is less than the threshold value and the surface profile recurs. When $R_{i,j} = 0$, the gap between two points on the surface contour is larger than the threshold and there is no recurrence in the surface contour. The recurrence of surface contours indicates that the greater the periodicity of the contours, the greater the predictability and the better the surface quality. The recursion graphs visualize this binary symmetric matrix. When $R_{i,j} = 1$, the recurrence graph is a black dot, and when $R_{i,j} = 0$, it is a white dot. Figure 13 illustrates the evolution of the recurrence graphs in the whole life cycle of region 4, which also reflects some of the raceway morphology. In Figure 13c, a wider white bar in the recurrence graphs indicates larger peaks and valleys on the raceway surface at this time, which corresponds to the surface profile of Figure 9(b3). The recurrence graphs in Figure 13i have significantly fewer black dots than the other recurrence graphs, indicating a dramatic deterioration of the 50 km raceway morphology.

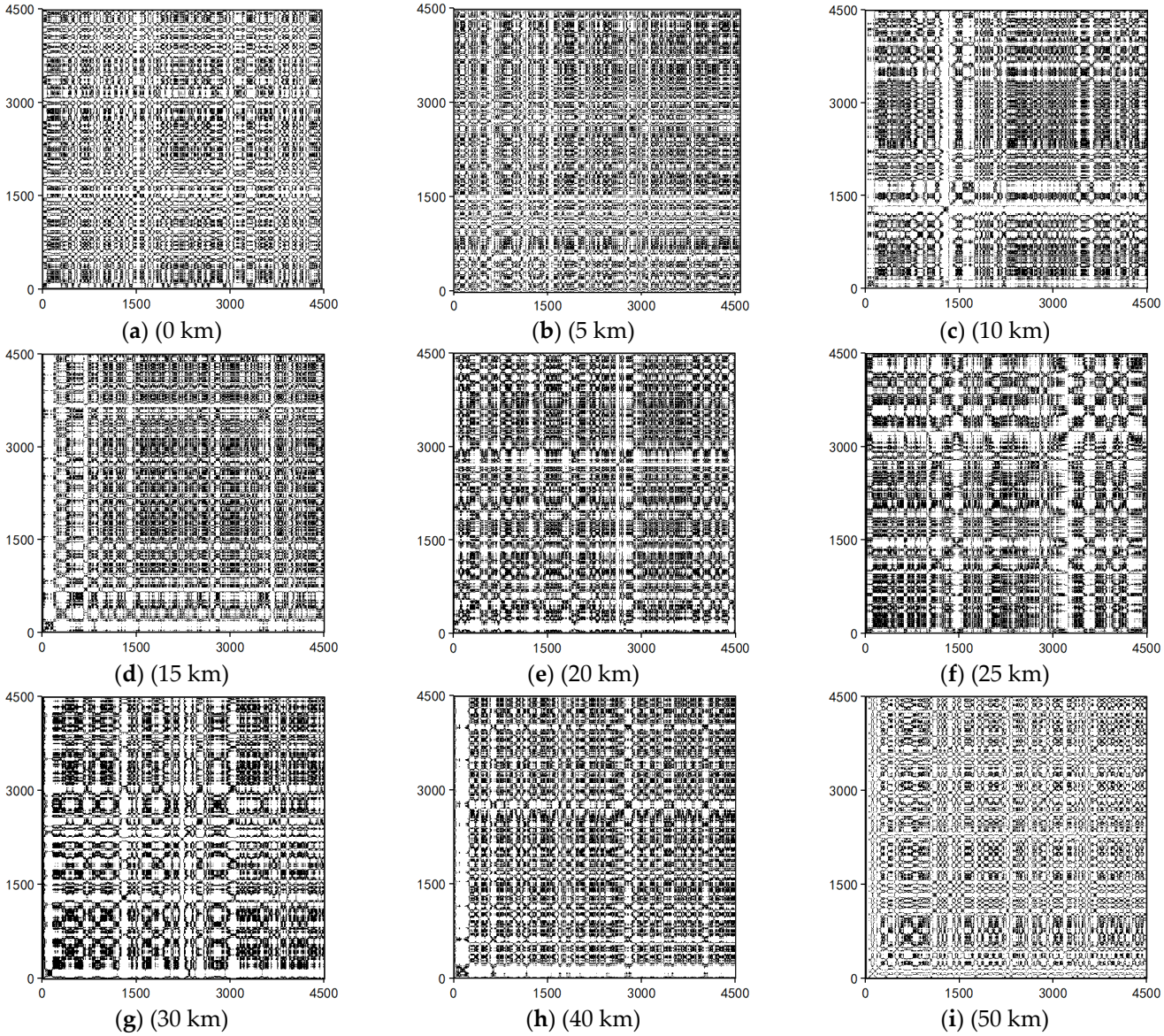


Figure 13. Recurrence plots of surface profiles during wear. (**a**) (0 km), (**b**) (5 km), (**c**) (10 km), (**d**) (15 km), (**e**) (20 km), (**f**) (25 km), (**g**) (30 km), (**h**) (40 km), (**i**) (50 km).

The recursion rate is the proportion of recurrence points among the total number of points in the entire recurrence plane. It quantitatively reflects the amount of similarity of the internal structure of the two-dimensional profile on the raceway surface [28] and is given by

$$Rr = \frac{1}{N^2}\sum_{i,j=1}^{N} R_{i,j} \tag{7}$$

Figure 14 shows the recurrence rates for the six regions, which are also fitted with a fifth-order polynomial. The fitting curves are similar to the fractal dimension D. Each first rises, then levels off, and finally drops sharply, showing an "inverted bathtub shape". This means that the number of recurrence points increases in the range 0–5 km and the surface quality improves. At 5–40 km, there is no significant change in the number of recurrence points and the surface quality of the raceway is in a stable state of dynamic equilibrium. At 40–50 km, the number of recurrence points decreases significantly, indicating that the surface quality of the raceway deteriorates sharply. This conclusion is consistent with the conclusions drawn from Ra, Rt, D, and the micrographs.

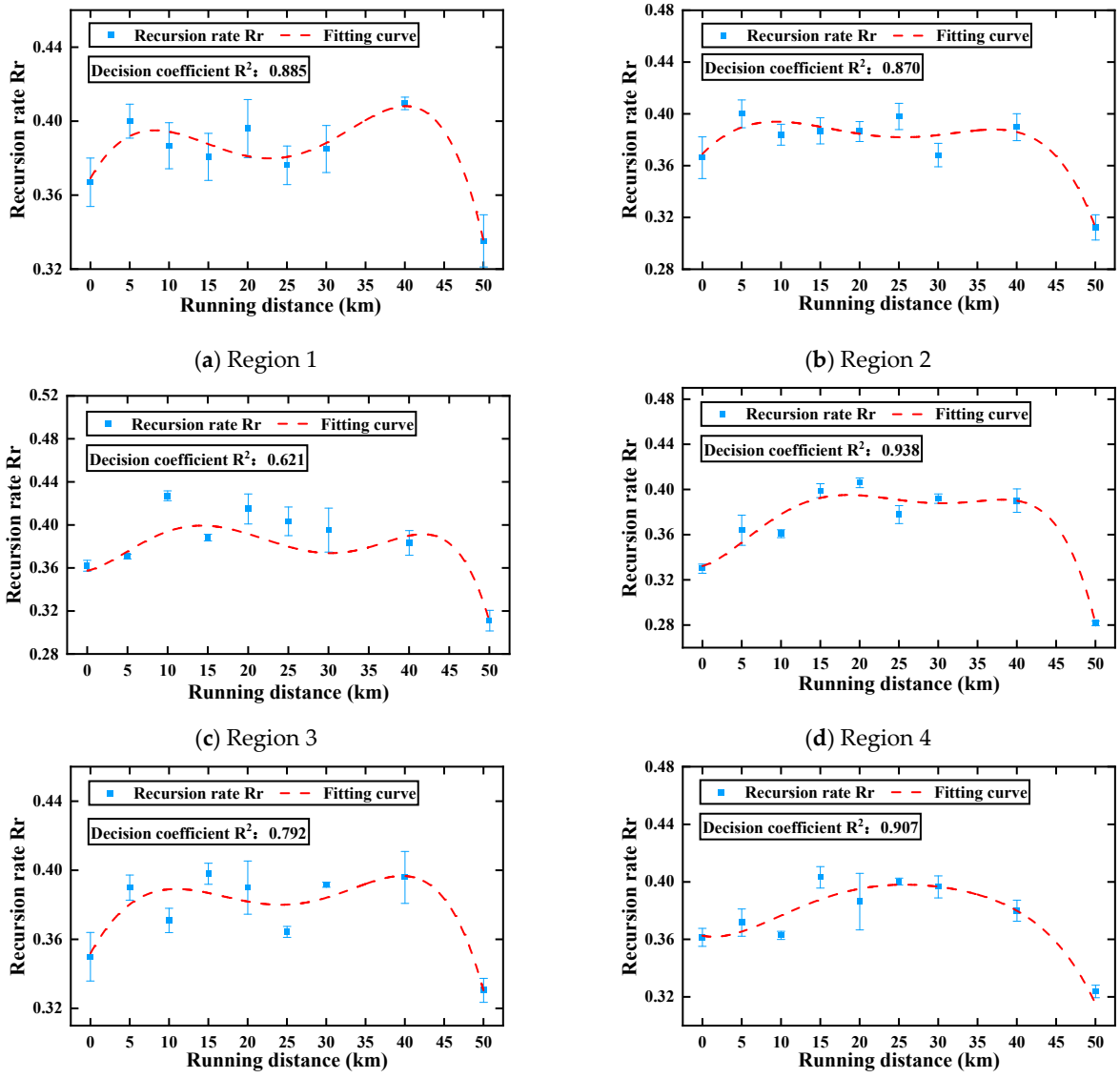


Figure 14. Evolution of recursion rate during wear. (**a**) Region 1, (**b**) Region 2, (**c**) Region 3, (**d**) Region 4, (**e**) Region 5, (**f**) Region 6.

4. Correlation Study

4.1. Establishing Correlation

The above analysis of the variation in parameters of the raceway morphology shows that the variational trends of Ra, Rt, D, and Rr have some similarity, being "bathtub-like" or "inverted bathtub-like". In this section, we take raceway 2 as an example and discuss the correlation between the degradation of the preload drag force of the LMRB and the parameter curves of the raceway morphology. To facilitate the analysis, we introduce the degradation rate τ defined as

$$\tau = \frac{F_{i-1} - F_i}{F_0} \times 100\% \; i = 0, 1, 2, \ldots \tag{8}$$

where F_i is the preload drag force after the ith run, and F_0 is the initial preload drag force of the LMRB.

Figure 15 shows the variational trends of τ in relation to the variations of the four parameters. For 0–5 km, τ is the highest and reaches 38.1%. At this time, Ra decreases slightly, the recurrence rate Rr and fractal dimension D increase to different degrees, and D changes the most. For 5–40 km, τ stabilizes below 5%, and Ra, Rr, and D all fluctuate in a small range. For 40–50 km, τ is negative and the LMRB can be judged as failing. At this time, Ra significantly increases and Rr and D significantly decrease. This verifies that there is a relation between the drag force of the LMRB and the raceway morphology. The four characteristic parameters reflect the degradation state of the preload drag force.

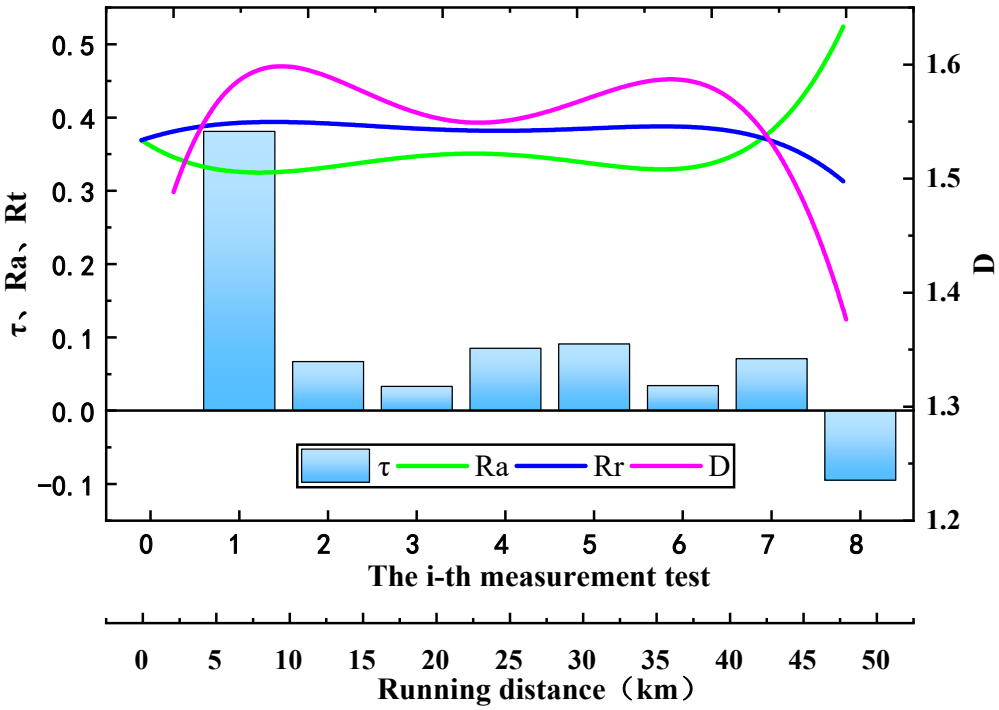


Figure 15. Characteristic parameters of raceway morphology and degradation rate of preload drag force during wear.

4.2. Gray Correlation

Gray correlation is a method that describes the strength, magnitude, and order of relationships among quantities or system factors. The degree of correlation is high if the shapes of the time series curves characterizing these factors are similar to each other; otherwise, the degree of correlation is low [29]. The correlation between each characteristic parameter and performance degradation was ranked using gray correlation. The response to the preload drag force is stronger when the correlation is higher [30,31].

The two data series are

$$X_1 = (x_1(1), x_1(2), \ldots, x_1(\mathrm{n})) \tag{9}$$

$$X_2 = (x_2(1), x_2(2), \ldots, x_2(\mathrm{n})) \tag{10}$$

There may be different unit magnitudes between data series, so the quantities first need to be made dimensionless as follows:

$$\hat{X}_1 = (\hat{x}_1(1), \hat{x}_1(2), \ldots, \hat{x}_1(\mathrm{n})) \tag{11}$$

$$\hat{X}_2 = (\hat{x}_2(1), \hat{x}_2(2), \ldots, \hat{x}_2(\mathrm{n})) \tag{12}$$

The correlation is

$$\gamma(\hat{X}_1, \hat{X}_2) = \frac{\min\limits_n |\hat{x}_1(\mathrm{n}) - \hat{x}_2(\mathrm{n})| + \zeta \cdot \max\limits_n |\hat{x}_1(\mathrm{n}) - \hat{x}_2(\mathrm{n})|}{|\hat{x}_1(\mathrm{n}) - \hat{x}_2(\mathrm{n})| + \max\limits_n |\hat{x}_1(\mathrm{n}) - \hat{x}_2(\mathrm{n})|} \tag{13}$$

where ζ is the coefficient of resolution; $\zeta \in (0, 1)$, so we let $\zeta = 0.5$.

The calculation results are shown in Table 3.

Table 3. Gray correlation degree.

Region / γ	Region 1	Region 2	Region 3	Region 4	Region 5	Region 6	Average Value
γ (F, Ra)	0.649	0.648	0.634	0.647	0.656	0.635	0.645
γ (F, Rt)	0.668	0.652	0.658	0.626	0.678	0.659	0.657
γ (F, D)	0.718	0.717	0.725	0.711	0.721	0.717	0.718
γ (F, Rr)	0.730	0.733	0.726	0.696	0.720	0.725	0.722

The average correlations between the changes in the four characteristic parameters (Ra, Rt, D, and Rr) and the degradation of the preload drag force are 0.645, 0.657, 0.718, and 0.722, respectively. Thus, the decreasing order of correlation between these four parameters and the preload drag force mapping is Rr, D, Rt, and Ra.

5. Preload Prediction

As shown in Section 4, the correlation between Rr and the degradation of the preload drag force is the strongest. Therefore, in this section, by using the Gaussian process regression theory, a regression model of the preload drag force is constructed on the basis of the rolling track topography of LMRB.

5.1. Gaussian Regression Process Model of Preload Drag Force

The Gaussian process regression (GPR) model is a non-parametric random process regression subject to Gaussian distribution. For a given training set $D = \{(x_i, y_i)\}_{i=1}^{N} = \{x, y\}$, where $x_i \in R^p$ represents the p-dimensional input vector, $x = \{x_1, x_2, \ldots, x_N\}$ is the $p \times N$-dimensional input matrix, $y_i \in R$ is the corresponding output scalar, and y is the output vector. In this paper, the Gaussian process regression model is used to establish the mapping relationship between the recurrence rate (Rr) and the preload drag force via learning samples. The simplified regression model is:

$$y = f(x) + \varepsilon \tag{14}$$

where ε is the noise or residual with a Gaussian distribution with variance δ_n^2:

$$\varepsilon \approx N(0, \delta_n^2) \tag{15}$$

The regression function $f(x)$ is a Gaussian process which can be described by its mean function $m(x)$ and covariance function $k(x, x')$ as:

$$f(x) \sim GP\big(m(x), k\big(x, x'\big)\big) \tag{16}$$

$$m(x) = E[f(x)] \tag{17}$$

$$k\big(x, x'\big) = E[(f(x) - m(x))\big(f\big(x'\big) - m\big(x'\big)\big)^T] \tag{18}$$

To simplify the calculation process, the mean function is usually taken as zero. After training with the real data obtained through the experiment, the prior distribution of the output value y is obtained as:

$$y \sim N(0, k\big(x, x'\big) + \delta_n^2 I) \tag{19}$$

The joint distribution of any finite random variable in the Gaussian process obeys the Gaussian distribution. Therefore, based on the new input test sample x^*, the joint distribution of the predicted output y^* and the output y also obeys the Gaussian distribution, namely:

$$\begin{pmatrix} y \\ y^* \end{pmatrix} \sim N\left(0, \begin{bmatrix} k(x,x) + \delta_n^2 I & k(x,x^*) \\ k(x^*,x) & k(x^*,x^*) \end{bmatrix}\right) \tag{20}$$

where $k(x, x)$ is the covariance matrix of the input sample x; $k(x, x^*) = k(x^*, x)^T$ is the given new input value x^* and training Covariance matrix between input values x; $k(x^*, x^*)$ is the variance of the given new input value x^*.

The posterior distribution of y^* is:

$$p(y^*|x^*, x, y) = N(m(y^*), cov(y^*)) \tag{21}$$

where the mean $m(y^*)$ and variance $cov(y^*)$ of y^* can be obtained as:

$$m(y^*) = k(x^*, x)[k(x, x) + \delta_n^2 I]^{-1} y \tag{22}$$

$$cov(y^*) = k(x^*, x) - k(x^*, x)[k(x, x) + \delta_n^2 I]^{-1} k(x^*, x)^T \tag{23}$$

Take the raceway surface recurrence rate as the input of the regression model and the preload drag force as the output of the model. RSME and R^2 can be used to indicate the confidence of the regression prediction value to the measured data.

5.2. Gaussian Regression Model Training and Prediction Analysis

5.2.1. Gaussian Regression Model Training

To increase the training accuracy of the gaussian regression model, 302 data points are extracted from the fitting curves of the recursion rate and the preload drag force shown in Figures 7 and 14. Import the collected training data into MATLAB for regression model training with five-fold cross-validation to prevent the overfitting. The basic and kernel function, the regression model evaluation indicator, the square root error RMSE and average error MAE are shown in Table 4. As shown in Figure 16a, the fitted preload drag force is in good agreement with the true result, which indicates the effectiveness of the training process.

Table 4. The parameters of the model and the training result.

Category \ Parameters	Base Function	Kernel Function	RMSE	R^2
GPR	Constant	Matern 5/2	0.00935	1.00

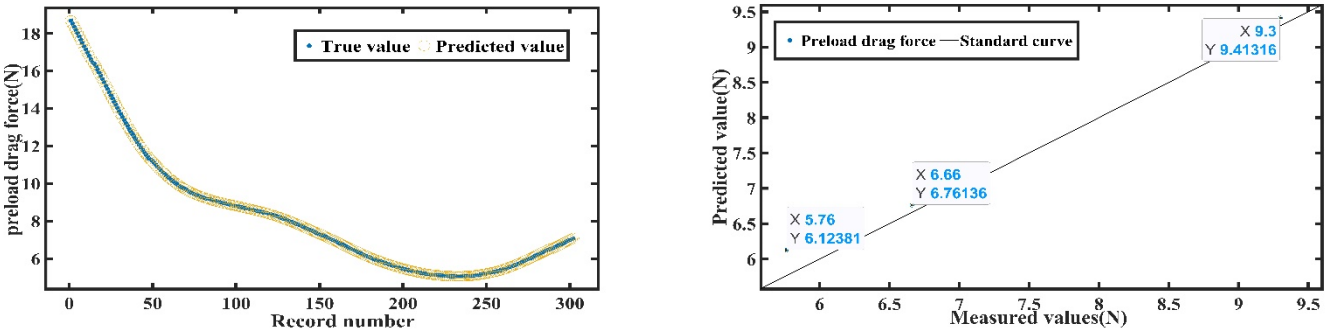


Figure 16. The training results and test results of the model. (**a**) Training results, (**b**) Testing results.

5.2.2. Prediction and Test Comparison of Preload Drag Force

As shown in Figure 16b, the predicted preload drag force is quite close to the standard curve. As shown in Table 5, the accuracies of prediction results of the three sets are 93.75%, 98.5%, and 98.8%, respectively, which validates the accuracy of the proposed model.

Table 5. Predicted values versus measured values.

Test Groups / Data	Region 1	Region 2	Region 3
Measured value	5.76	6.66	9.30
Predicted value	6.12	6.76	9.41
Accuracy	93.75%	98.5%	98.8%

6. Conclusions

This study investigated the correlation between the degradation of LMRB performance and the change in morphology of the raceway surface of a type 35 LMRB. The LMRB was loaded at 60% C and 50 m/min, and its preload drag force and change in raceway morphology were measured. The two-dimensional profile of the raceway surface was characterized using statistical parameters, single fractals, and recursive analysis. The two-dimensional profile parameters of the raceway surface were correlated with the degradation in preload drag force. Finally, a regression model of the preload drag force is constructed on the basis of the rolling track topography of LMRB. The following are the highlights and conclusions of the study:

a. The degradation in preload drag force of the LMRB is divided into three stages: rapid descent, slow descent, and failure.
b. Comparing the variation in preload drag force with the microscopic images and two-dimensional profile of the raceway surface shows that the raceway morphology reflects the degradation state of its preload drag force.
c. The four parameters Ra, Rt, D, and Rr effectively represent the variational law of raceway morphology. The variational trends of Ra and Rt are "bathtub shaped", and the variational trends of the fractal dimension D and recurrence rate Rf show an "inverted bathtub shape". This conclusion provides a new way to monitor the degradation of the preload drag force of an LMRB.
d. Gray correlation analysis of the degradation trend of the preload drag force yields correlations of 0.645, 0.657, 0.718, and 0.722 for the four characteristic parameters Ra, Rt, D, and Rr, respectively. Rr was recognized as optimal characterizing parameter.
e. By using the Gaussian process regression theory, a regression model of the preload drag force is constructed on the basis of the rolling track topography of LMRB. The accuracies of prediction results of the three sets are 93.75%, 98.5%, and 98.8%, respectively, which validates the accuracy of the proposed model. This model describe

in this paper can be utilized efficiently for the prediction of LMRB preload drag force degradation based on rolling morphology.

Author Contributions: Conceptualization, L.L. and H.C.; methodology, H.C. and Z.L.; software, H.C. and W.-P.L.; formal analysis, H.C. and W.-P.L.; investigation, H.C. and W.-P.L.; resources, H.-T.F. and C.-G.Z.; data curation, H.C. and Z.L.; writing—original draft preparation, H.C. and W.-P.L.; writing—review and editing, L.L., H.C. and W.-P.L.; visualization, H.C. and W.-P.L.; supervision, Y.L., H.-T.F. and C.-G.Z.; project administration, Y.L., H.-T.F. and C.-G.Z.; funding acquisition, Y.L., H.-T.F. and C.-G.Z. All authors have read and agreed to the published version of the manuscript.

Funding: This project is supported by the National High Quality Development Projects of China: (Grant No. TC210H038-002), the National Natural Science Foundation of China (Grant No. 51905274), and the National Science and Technology Major Projects of China (Grant No. 2018ZX04039001, 2017ZX04011001, 2012ZX04002021). Open Fund of Key Laboratory of CNC Equipment Reliability of Jilin University (Grant No. 202105).

Data Availability Statement: The data presented in this study are available on request from the corresponding author. The data are not publicly available due to privacy.

Conflicts of Interest: The authors declare no conflict of interest.

References

1. Tong, V.; Khim, G.; Hong, S.; Park, C.H. Construction and validation of a theoretical model of the stiffness matrix of a linear ball guide with consideration of carriage flexibility. *Mech. Mach. Theory* **2019**, *140*, 123–143. [CrossRef]
2. Chen, C.; Li, B.; Guo, J.; Liu, Z.; Qi, B.; Hua, C. Bearing life prediction method based on the improved FIDES reliability model. *Reliab. Eng. Syst. Saf.* **2022**, *227*, 108746. [CrossRef]
3. Sun, W.; Kong, X.; Wang, B.; Li, X. Statics modeling and analysis of LMRB way considering rolling balls contact. Proceedings of the Institution of Mechanical Engineers. *Part C J. Mech. Eng. Sci.* **2015**, *229*, 168–179. [CrossRef]
4. Li, D.; Liu, X.; Li, L.; Guo, G. Influence of Geometric Parameters on Lubrication Performance of Rolling Linear Guides Considering Stiffness Effects. *J. Mech. Eng.* **2021**, *57*, 100–108. [CrossRef]
5. Han, J.; Dai, L. Research on Interchangeability Technology of Low Preload Rolling Linear Guide Pair. *Sci. Technol. Vis.* **2018**, *25*, 23–24+53. [CrossRef]
6. Qi, B.; Zhao, J.; Chen, C.; Song, X.; Jiang, H. Accuracy decay mechanism of ball screw in CNC machine tools for mixed sliding-rolling motion under non-constant operating conditions. *Int. J. Adv. Manuf. Technol.* **2022**. [CrossRef]
7. Gu, Q.; Liang, Y.; Ren, X.; Feng, H.; Zhou, C. Relation between Friction Force and Static Stiffness of Roller Guide. *Modul. Mach. Tool Autom. Manuf. Tech.* **2020**, 67–71+75. [CrossRef]
8. Ren, S.; Zhou, C.; Ye, K.; Feng, H.-T.; Zhang, Y.-S. Calculating and Experiment Study on Friction Coefficient of LMRB. *Tribology* **2022**, *42*, 305–313. [CrossRef]
9. Cheng, D.J.; Yang, W.S.; Park, J.H.; Park, T.J.; Kim, S.J.; Kim, G.H.; Park, C.H. Friction experiment of linear motion roller guide THK SRG25. *Int. J. Precis. Eng. Manuf.* **2014**, *15*, 545–551. [CrossRef]
10. Oh, K.; Khim, G.; Park, C.; Chung, S.C. Explicit modeling and investigation of friction forces in linear motion ball guides. *Tribol. Int.* **2019**, *129*, 16–28. [CrossRef]
11. Zhou, C.; Ren, S.; Feng, H.; Shen, J.-W.; Zhang, Y.-S.; Chen, Z.T. A new model for the preload degradation of LMRB. *Wear* **2021**, *482–483*, 203963. [CrossRef]
12. Huang, H.; Gao, H.; Xu, M.; Zhang, X.; Guo, L. Performance Degradation Evaluation Method of CNC Machine Tool Spindle System. *J. Vib. Meas. Diagn.* **2013**, *33*, 646–652+726. [CrossRef]
13. Yang, X.; Wu, J.; Ma, J. Rolling bearing performance degradation assessment method based on dispersion entropy and cosine Euclidean distance. *J. Electron. Meas. Instrum.* **2020**, *34*, 15–24. [CrossRef]
14. Cheng, R.; Ou, Q.; Feng, H. Study on the Influence of Preload to Vibration of Roller Linear Guide Pairs. *Modul. Mach. Tool Autom. Manuf. Tech.* **2018**, *03*, 11–13+18. [CrossRef]
15. Liu, X. Correlation analysis of surface topography and its mechanical properties at micro and nanometre scales. *Wear* **2013**, *305*, 305–311. [CrossRef]
16. Valtonen, K.; Ratia, V.; Ojala, N.; Kuokkala, V.T. Comparison of laboratory wear test results with the in-service performance of cutting edges of loader buckets. *Wear* **2017**, *388–389*, 93–100. [CrossRef]
17. Zhang, S.; Sun, Z.; Guo, F. Investigation on wear and contact fatigue of involute modified gears under minimum quantity lubrication. *Wear* **2021**, *484–485*, 204043. [CrossRef]
18. Hanrahan, B.; Misra, S.; Waits, C.M.; Ghodssi, R. Wear mechanisms in microfabricated ball bearing systems. *Wear* **2015**, *326–327*, 1–9. [CrossRef]
19. Zuo, X.; Tan, Y.; Zhou, Y.; Zhu, H.; Fang, H. Multifractal analysis of three-dimensional surface topographies of GCr15 steel and H70 brass during wear process. *Measurement* **2018**, *125*, 196–218. [CrossRef]

20. Xiong, Y.; Wang, W.; Shi, Y.; Jiang, R.; Shan, C.; Liu, X.; Lin, K. Investigation on surface roughness, residual stress and fatigue property of milling in-situ TiB2/7050Al metal matrix composites. *Chin. J. Aeronaut.* **2021**, *34*, 451–464. [CrossRef]
21. Zhu, H.; Zuo, X.; Zhou, Y. Recurrence evolvement of brass surface profile in lubricated wear process. *Wear* **2016**, *352–353*, 9–17. [CrossRef]
22. Xu, L.; Li, Y. Modeling of a deep-groove ball bearing with waviness defects in planar multibody system. *Multibody Syst. Dyn.* **2014**, *33*, 229–258. [CrossRef]
23. Wang, X.; Feng, H.; Zhou, C.; Chen, Z.T.; Xie, J.L. A New Two-Stage Degradation Model for the Preload of Linear Motion Ball Guide Considering Machining Errors. *J. Tribol.* **2022**, *144*, 051202. [CrossRef]
24. Zhu, Q.; Feng, H.; Ou, Y. Research status and ideas of rolling linear guide life test methods. *Mach. Manuf. Autom.* **2015**, *44*, 5. (In Chinese)
25. Xu, F.; Zhang, W.; Du, Y.; Song, C.; Shan, R.; Zhu, M. Analysis of Surface Integrity of EA4T Axle Being Processed in Different Technologies. *Surf. Technol.* **2017**, *46*, 277–282. [CrossRef]
26. Ge, S. Research on Fractal Features and Fractal Expression of Rough Surface. *Tribology.* **1997**, *17*, 74–81.
27. Ganti, S.; Bhushan, B. Generalized fractal analysis and its applications to engineering surfaces. *Wear* **1995**, *180*, 17–34. [CrossRef]
28. Izquierdo, S.; López, C.I.; Valdés, J.R.; Miana, M.; Martínez, F.J.; Jiménez, M.A. Multiscale characterization of computational rough surfaces and their wear using self-affine principal profiles. *Wear* **2012**, *274–275*, 1–7. [CrossRef]
29. Zuo, X.; Zhu, H.; Zhou, Y.; Ding, C. Monofractal and multifractal behavior of worn surface in brass–steel tribosystem under mixed lubricated condition. *Tribol. Int.* **2016**, *93*, 306–317. [CrossRef]
30. Chao, P.; Qide, T.; Guowei, C. Hybrid Short-Term Wind Speed Prediction Model by COA-SVR Based on Recursive Quantitative Analysis. *Power Syst. Technol.* **2018**, *42*, 2373–2381. [CrossRef]
31. Zhou, W.; Zeng, B. A Research Review of Grey Relational Degree Model. *Stat. Decis.* **2020**, *36*, 29–34. [CrossRef]